

Dynamic electric potential redistribution and its influence on the development of a dielectric barrier plasma jet

This article has been downloaded from IOPscience. Please scroll down to see the full text article.

2012 Plasma Sources Sci. Technol. 21 034009

(<http://iopscience.iop.org/0963-0252/21/3/034009>)

View [the table of contents for this issue](#), or go to the [journal homepage](#) for more

Download details:

IP Address: 131.84.11.215

The article was downloaded on 10/05/2012 at 01:21

Please note that [terms and conditions apply](#).

Report Documentation Page				Form Approved OMB No. 0704-0188	
Public reporting burden for the collection of information is estimated to average 1 hour per response, including the time for reviewing instructions, searching existing data sources, gathering and maintaining the data needed, and completing and reviewing the collection of information. Send comments regarding this burden estimate or any other aspect of this collection of information, including suggestions for reducing this burden, to Washington Headquarters Services, Directorate for Information Operations and Reports, 1215 Jefferson Davis Highway, Suite 1204, Arlington VA 22202-4302. Respondents should be aware that notwithstanding any other provision of law, no person shall be subject to a penalty for failing to comply with a collection of information if it does not display a currently valid OMB control number.					
1. REPORT DATE MAY 2012		2. REPORT TYPE		3. DATES COVERED 00-00-2012 to 00-00-2012	
4. TITLE AND SUBTITLE Dynamic Electric Potential Redistribution And Its Influence On The Development Of A Dielectric Barrier Plasma Jet				5a. CONTRACT NUMBER	
				5b. GRANT NUMBER	
				5c. PROGRAM ELEMENT NUMBER	
6. AUTHOR(S)				5d. PROJECT NUMBER	
				5e. TASK NUMBER	
				5f. WORK UNIT NUMBER	
7. PERFORMING ORGANIZATION NAME(S) AND ADDRESS(ES) Air Force Research Laboratory, 2645 5th St., Wright Patterson Air Force Base, OH, 45433				8. PERFORMING ORGANIZATION REPORT NUMBER	
9. SPONSORING/MONITORING AGENCY NAME(S) AND ADDRESS(ES)				10. SPONSOR/MONITOR'S ACRONYM(S)	
				11. SPONSOR/MONITOR'S REPORT NUMBER(S)	
12. DISTRIBUTION/AVAILABILITY STATEMENT Approved for public release; distribution unlimited					
13. SUPPLEMENTARY NOTES Plasma Sources Sci. Technol. 21 (2012) 034009 (11pp)					
14. ABSTRACT We investigate the initiation and development of a streamer-like plasma jet generated in a single-electrode dielectric barrier configuration at atmospheric pressure. The influence of dielectric boundary conditions on discharge propagation dynamics, morphology and current distribution was studied using spatially and temporally resolved emission spectroscopy and wide-bandwidth current measurements. A Phantom high-frame-rate camera system was used to visualize discharge inception as a function of pulse repetition frequency, which was varied between 1 and 20 kHz. At discharge inception, with the copper ring anode located 20mm behind the capillary tip, the discharge propagated along the 2mm diameter inner wall of the glass capillary regardless of pulse repetition frequency. The steady-state morphology remained annular below 6 kHz, but gradually transitioned to an axial morphology with the expansion of a dark wall sheath towards the anode as the pulse repetition frequency was increased to 10 kHz. In the axial mode, the ionization front steadily decelerated with a corresponding decrease in peak emission intensity, while emission from the residual plasma channel increased. This indicated a dynamic redistribution of electric potential from the ionization front into the residual plasma channel that was attributed to charge accumulation on the dielectric surface between discharge pulses.					
15. SUBJECT TERMS					
16. SECURITY CLASSIFICATION OF:			17. LIMITATION OF ABSTRACT Same as Report (SAR)	18. NUMBER OF PAGES 13	19a. NAME OF RESPONSIBLE PERSON
a. REPORT unclassified	b. ABSTRACT unclassified	c. THIS PAGE unclassified			

Dynamic electric potential redistribution and its influence on the development of a dielectric barrier plasma jet

Brian L Sands^{1,4}, Shih K Huang², Jared W Speltz², Matthew A Niekamp², Jacob B Schmidt^{3,4} and Biswa N Ganguly⁴

¹ UES, Inc. 4401 Dayton-Xenia Rd. Dayton, OH 45432, USA

² Wright State University, Department of Mechanical and Materials Engineering, 3640 Colonel Glenn Hwy., Dayton, OH 45435, USA

³ Spectral Energies, LLC. 5100 Springfield St. Suite 301, Dayton, OH 45431, USA

⁴ Air Force Research Laboratory, 2645 5th St. Wright Patterson Air Force Base, OH 45433, USA

E-mail: brian.sands@wpafb.af.mil

Received 27 October 2011, in final form 29 February 2012

Published 2 May 2012

Online at stacks.iop.org/PSST/21/034009

Abstract

We investigate the initiation and development of a streamer-like plasma jet generated in a single-electrode dielectric barrier configuration at atmospheric pressure. The influence of dielectric boundary conditions on discharge propagation dynamics, morphology and current distribution was studied using spatially and temporally resolved emission spectroscopy and wide-bandwidth current measurements. A Phantom high-frame-rate camera system was used to visualize discharge inception as a function of pulse repetition frequency, which was varied between 1 and 20 kHz. At discharge inception, with the copper ring anode located 20 mm behind the capillary tip, the discharge propagated along the 2 mm diameter inner wall of the glass capillary regardless of pulse repetition frequency. The steady-state morphology remained annular below 6 kHz, but gradually transitioned to an axial morphology with the expansion of a dark wall sheath towards the anode as the pulse repetition frequency was increased to 10 kHz. In the axial mode, the ionization front steadily decelerated with a corresponding decrease in peak emission intensity, while emission from the residual plasma channel increased. This indicated a dynamic redistribution of electric potential from the ionization front into the residual plasma channel that was attributed to charge accumulation on the dielectric surface between discharge pulses.

(Some figures may appear in colour only in the online journal)

 Online supplementary data available from stacks.iop.org/PSST/21/034009/mmedia

1. Introduction

Dielectric barrier plasma jet devices, of the type described by Teschke *et al* [1], are capable of generating stable, nonequilibrium plasmas at atmospheric pressure over distances of several centimetres in air. These sources have generated significant interest for their potential to facilitate remote plasma processing applications under ambient conditions. The utility of this source is derived from its ability to generate reactive species *in situ* near the target substrate. This type of atmospheric pressure plasma jet (APPJ) is electrically similar to classical streamer discharge phenomena [2, 3] in

that it is generated from a highly localized, self-sustained ionization wave that rapidly propagates at speeds of order 10^7 cm s^{-1} [1, 4–7]. The use of a dielectric capillary to effuse a rare gas flow into ambient air also invokes similarities with conventional dielectric barrier discharge (DBD) devices.

The dielectric barrier plasma jet represents a hybrid between streamer corona and conventional DBD sources. For positive-going applied voltages, the discharge initially develops in a similar way as a cathode-directed streamer discharge; that is, electrons generated in the leading ionization front are conducted along the residual plasma channel that completes the circuit between the powered electrode and the

advancing ionization front. The overall conductance of the residual plasma channel determines the minimum electric field required to maintain current continuity in the channel. This is the so-called ‘stability electric field’, which is at least an order of magnitude lower than the electric field at the ionization front [3, 8], but determines the extent of the propagating ionization front for a particular applied voltage [2]. In contrast to streamer corona and DBD sources operated in homogeneous media, the plasma channel conductance is more complex for plasma jet devices in part because the discharge propagates through a structured heterogeneous medium set up by the gradual entrainment of air into the core rare gas flow. This introduces a gradient in the local conductivity of the residual plasma channel, which changes the distribution of electric potential in the channel as a higher electric field is required to maintain current continuity when more air is incorporated. Thus, the length of the plasma jet in air is interdependent on the applied voltage and the gas flow rate [9, 10]. The presence of the cylindrical dielectric barrier can also modify the distribution of electric potential in the plasma channel via the accumulation of space charge at the surface. This leads to a dependence on the specific electrode configuration, which has been shown to have a significant impact on the power coupled into the plasma jet [11]. Experiments that have compared the properties of plasma jets inside the dielectric capillary and in ambient air have focused on the propagation dynamics and morphology of the discharge. The leading ionization front has been observed to propagate more slowly inside the capillary [9, 12, 13] and consistently accelerate upon exiting the capillary into ambient air [7, 9, 12–17]. This observation has been reproduced in recent numerical simulations [18, 19]. The discharge morphology has often been observed to be annular for helium plasma jets in ambient air [9, 13], but has appeared annular or filamentary depending on the dielectric boundary conditions inside the capillary [13].

The unique characteristics of dielectric barrier plasma jet devices are not adequately represented by conventional models for cathode-directed streamer discharges or traditional DBD sources. Current efforts at modelling this new class of dielectric barrier discharge have focused on the development of a single breakdown pulse under varying assumptions of plasma chemistry and boundary conditions [18–23]. To complement these efforts, this paper aims to provide a detailed experimental account of the role of changing dielectric boundary conditions on the development of the streamer-like discharge that forms the plasma jet in the multi-kHz regime, from initial breakdown through the formation of the ‘steady-state’ discharge. The discharge was generated in a single-electrode configuration with the position of the anode relative to the capillary tip variable. A unipolar pulsed voltage was used to excite the plasma jet with a repetition frequency that was varied between 1 and 20 kHz. As a starting point, we utilized a Phantom high-frame-rate camera [24], synchronized to the applied voltage trigger pulse, to visualize the inception behaviour of the discharge as a function of pulse repetition frequency. The image sequences show that the initial breakdown mostly follows the dielectric wall of the capillary regardless of repetition frequency, similar to what was

shown in [20]. At repetition frequencies < 6 kHz, the steady-state morphology remained annular. However, a transition was observed between 6 and 10 kHz that was marked by the appearance of a dark wall sheath that expanded from the capillary tip towards the anode with increasing pulse frequency, resulting in a shift to an axial morphology above 10 kHz. Using a combination of spatially and temporally resolved optical emission and wide-bandwidth current measurements, this transition was correlated with a significant perturbation of the ionization front propagation velocity that shifted towards the anode along with the peak emission intensity and peak current. Where the discharge morphology was predominantly axial, significant emission was observed in the residual plasma channel from the $3^3\text{D}-2^3\text{P}$ and $3^3\text{S}-2^3\text{P}$ He transitions that normally are not excited in the low reduced electric field behind the ionization front. The ionization front emission intensity and local propagation speed also steadily decreased within this region. These observations are attributed to a build-up of space charge along the dielectric surface following the initial breakdown pulse that dynamically redistributes electric potential from the ionization front to the residual plasma channel. The discharge propagation dynamics can be used as a sensitive indicator for changes in this potential distribution, whether it be from surface charging or changes in the local gas conductivity. The results are presented in three sections, starting with the inception behaviour of the plasma jet visualized with the Phantom high-frame-rate camera, followed by a detailed characterization of the discharge in the annular mode at a repetition frequency of 2 kHz, and finally how these characteristics changed as the repetition frequency was increased.

2. Experiment

Our experimental configuration is depicted in figure 1. The plasma jet was generated from a Pyrex capillary with a 2 mm inner diameter and a 3 mm outer diameter wrapped with a single 2 cm wide copper-foil electrode to power the discharge. A distant ground reference was located upstream (~ 20 cm) though this had a negligible impact on the experiment. The copper electrode was powered with a unipolar positive voltage pulse train delivered from a high-voltage MOSFET switch (Behlke HTS-150). The pulse repetition frequency was varied between 1 and 20 kHz. An example of the voltage waveform used for most of the measurements in this paper is shown as an inset of figure 1. The risetime of the voltage pulse was 20 ns. The switch had a fixed ontime of 120 ns but due to the high RC time constant in the circuit, the voltage decayed over $\sim 8 \mu\text{s}$. This kept the applied voltage from changing significantly while the ionization front was propagating. The data in this paper were acquired with 12 kV applied voltage. To facilitate comparison with other plasma jet experiments, helium was used as the carrier gas. The flow rate was kept constant at 2 standard l/min (slm).

To visualize the inception behaviour of the discharge, broadband emission was acquired using a high-frame-rate CMOS camera from Vision Research Inc., the Phantom V7, hereafter referred to as the Phantom camera [24]. The CMOS

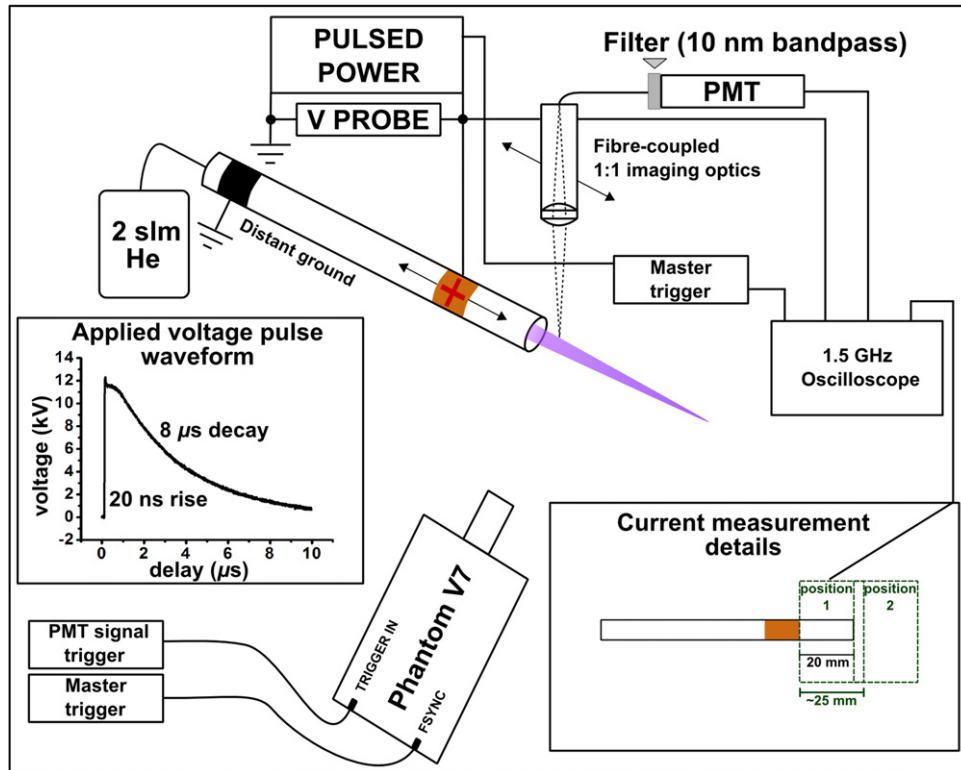


Figure 1. Schematic diagram of the experimental configuration. The insets show the typical applied voltage waveform and positions used for the current measurements.

detector was coupled to a 105 mm, $f/4.5$ UV Nikkor lens. Imaging was synchronized to the master trigger pulse that gated the high-voltage switch via a delay generator to compensate for cable and internal signal delays. An optical detector, mounted near the anode and fibre-coupled to a photomultiplier tube (PMT), was used to define the start of the image sequence. The camera imaged continuously until a ‘first light’ signal was received from the PMT, then imaging was terminated after a predefined number of pulses. A pixel response calibration was performed before each acquisition to ensure maximum dynamic range. The exposure time for each pulse was $5\ \mu\text{s}$, sufficient to track the full development of the discharge. About 2000 consecutive exposures were acquired to ensure that a steady state had been reached.

A PMT (Hamamatsu R-928) was used to acquire spatially and temporally resolved emission from the discharge. This was fibre-coupled to movable detection optics that collected light from a $\sim 1\ \text{mm}$ spot on the capillary axis. Interference filters with a bandpass of 10 nm were used to isolate specific emission features. The PMT had a specified risetime of 2 ns. In order to more precisely measure the variation in emission intensity as the ionization front passed through the field of view of the detector, the effects of source jitter, albeit small for most dielectric barrier plasma jet devices with sufficient overvoltage, had to be mitigated. With a normal averaging of shot-to-shot emission traces, jitter in the inception delay tends to broaden the averaged profile and fine details may be obscured. To reduce this artefact, the emission traces were averaged by fitting the peak of each acquired trace and dynamically shifting them to the moving average delay. In this way, the

single-shot emission profile could be better preserved while simultaneously quantifying the jitter. Furthermore, to get an accurate measure of the discharge dynamics, it is important to track emission from the leading edge of the ionization front. Among the brightest transitions in a He plasma jet effused into air are $\text{N}_2\ (C^3\Pi_u)-(B^3\Pi_g)(0,0)$ at 337.1 nm, $\text{N}_2^+\ (B^2\Sigma_u)-(X^2\Sigma_g)(0,0)$ at 391.4 nm, $\text{He}\ (3^3D)-(2^3P)$ at 587.6 nm and $\text{He}\ (3^3S)-(2^3P)$ at 706.5 nm. Of these, the 587.6 and 706.5 nm emission lines from atomic He provided the most accurate signal from the ionization front. These lines are sensitive to the highest energy electrons that would be expected near the ionization front, due to high excitation threshold energies of 23.1 eV and 22.7 eV, respectively. Additionally, these lines are not as susceptible to excitation from pathways other than direct electron impact. For example, the 391.4 nm emission from N_2^+ was contaminated by Penning ionization from the 2^3S He metastable and the 337.1 nm emission from N_2 was vulnerable to both collisional energy transfer from other excited air species and lower energy electrons that persisted in the wake of the passing ionization front. Both of these effects broadened the respective temporal emission profiles and distorted the true location of the ionization front [14]. Between the 587.6 and 706.5 nm emission lines, the 587.6 nm line was the preferred choice to track the ionization front, when it was bright enough, since the 3^3S state spawning 706.5 nm emission is more likely to be collisionally and radiatively populated from the 3^3P state than the slightly higher energy 3^3D state [25]. These considerations are especially important near the anode and inside the capillary. Starting about 1 cm outside the capillary, air entrainment is sufficient such that emission from both

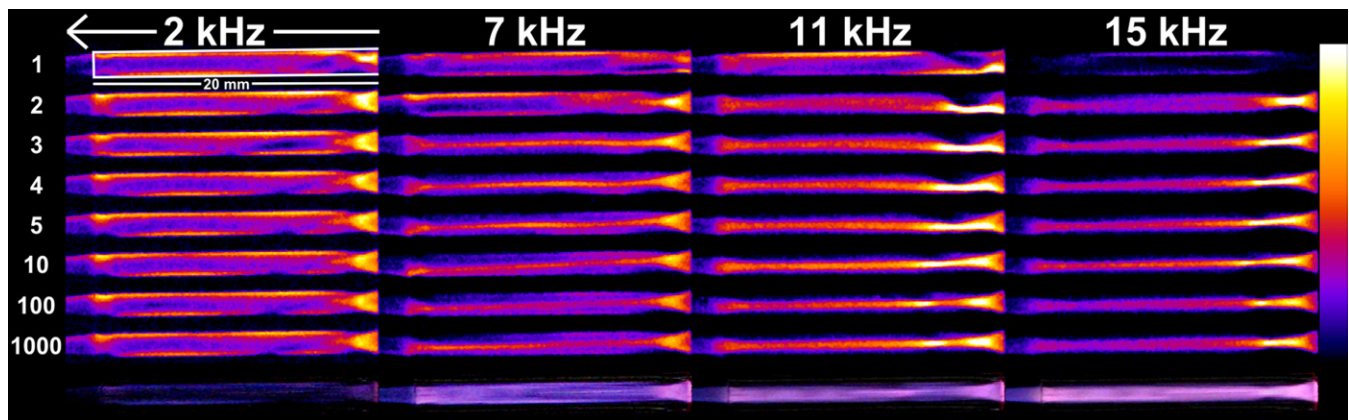


Figure 2. Image sequences from a Phantom high-frame-rate camera system synchronized to the applied voltage pulse train. Relative broadband emission is represented in false colour with the highest emission intensity represented by lighter colours. An outline of the capillary boundaries and indication of gas flow direction is shown on the first frame at 2 kHz. A true colour digital photograph is appended to the bottom of each sequence for reference. The frames are labelled with the pulse number starting with the initial breakdown pulse. The exposure time for each frame was $5 \mu\text{s}$. The morphology of the discharge at inception was always annular, regardless of pulse repetition frequency. Starting with the 7 kHz sequence, a transition was observed in the discharge morphology after the first pulse, from annular to axial with the development of a dark wall sheath that expanded from the capillary tip towards the anode with increased repetition frequency. Full image sequences showing the first 100 pulses are included online at stacks.iop.org/PSST/21/034009.

excited He and air species can track the ionization front well, owing to the increased quenching rate of excited states.

The discharge current was measured using a wide-bandwidth current monitor (Pearson model 6585). The 25 mm thick current monitor was placed in two positions to compare the total current (position 1 in figure 1) with the current generated primarily from outside the capillary (position 2 in figure 1). Although the current monitor had a large inner diameter of 5 cm, the capacitive perturbation due to its close proximity with the anode tended to increase the overall measured discharge current and reduce the apparent discharge inception delay. For example, we measured the current along the supply line from the high-voltage switch to the anode to be about a factor of three larger with the current monitor in place at position 1 than without. This is an important consideration since many groups have used a similar approach to measuring the discharge current, which may complicate quantitative comparisons with model calculations. Since *relative* trends in the measured current are emphasized here, this perturbation does not impact the interpretation of our results. However, care was taken when comparing current measurements with other data acquired without the current monitor, such as PMT emission measurements. For both the PMT and current measurements, the backgrounds, measured with no plasma, were subtracted from the raw traces to eliminate switching transients. The displacement current, taken from the current monitor background, was used as a common timing reference.

3. Results

3.1. Discharge inception

A visualization of discharge inception for this plasma jet device is shown in figure 2. This figure provides an overview of the effects described in this paper. The labelled image sequences were acquired with the Phantom camera system

as described in section 2 and are displayed in false colour to emphasize the regions of highest relative emission intensity in each case. Each frame represents a single discharge pulse from the high-voltage pulse train that drives the plasma jet and is labelled sequentially starting from the first discharge pulse. The gas flow direction and an outline of the capillary boundary are shown at the top-left of the figure. A true colour digital photograph is appended to the bottom of each Phantom camera image sequence for reference. The most significant changes in the discharge morphology occurred in the first 5–10 pulses, followed by a more gradual stabilization phase. The effective steady-state behaviour is represented by the images shown at 1000 pulses after discharge inception. These can be compared with the true colour images. At 2 kHz, the steady-state discharge morphology was annular and was clearly highlighted by emission peaks near the anode and near the capillary tip. The discharge remained annular up to 6 kHz then gradually transitioned to an axial morphology coinciding with the appearance of a dark wall sheath that expanded from the capillary tip towards the anode as the repetition frequency was increased. The onset of this transition is shown in figure 2 at 7 kHz. Under our conditions, this transition occurred between 6 and 10 kHz. The discharge morphology was primarily axial for pulse repetition frequencies above 10 kHz and was marked by a shift of the dominant emission intensity towards the anode, which is visible in figure 2 from 11 to 15 kHz. Despite the final steady-state appearance, however, the discharge morphology at inception was always annular, regardless of pulse repetition frequency. The conditions at discharge inception more closely correspond to those reported in [20], which observed a similar annular discharge morphology in modelling and experiment at pulse frequencies up to 60 Hz. The steady-state discharge behaviour better reflected the behaviour at discharge inception at low repetition frequencies, up to 6 kHz under our experimental conditions. The following section focuses on the characteristics of this discharge source in this regime, including

the propagation dynamics and spatiotemporal distribution of relative emission intensity and current, at a fixed repetition frequency of 2 kHz.

3.2. Discharge characteristics at fixed frequency

The propagation dynamics of the streamer-like discharge that forms the plasma jet are shown in figure 3(a) for anode positions at -20 , -10 , -2 and 0 mm. The data are shown from the 706.5 nm He $3^3\text{S}-2^3\text{P}$ transition. To facilitate discussion of the results, positions on the capillary axis are parametrized by the variable z . The capillary tip is defined as $z = 0$; negative positions correspond to locations inside the capillary, and positive positions are outside the capillary. The delay times for arrival of the ionization front are plotted against the position of the PMT-coupled detection optics. The error bars quantify the temporal jitter at each point averaged over 100 pulses. A steeper local slope indicates a *slower* local propagation speed. For anode positions located along $-z$, the discharge dynamics were characterized by an initial acceleration within the first ~ 5 mm from the anode. This acceleration was amplified with the anode located at $z = -2$ mm but notably decreased when the anode was located at the capillary tip. At an anode position of $z = -20$ mm, following the initial acceleration, the ionization front propagated at a nearly constant speed before decelerating ~ 5 mm from the capillary tip. With the anode at $z = -10$ mm, the initial acceleration was immediately followed by deceleration near the capillary tip. In each of these cases, the ionization front propagated *faster* in ambient air than inside the capillary.

Figure 3(b) shows temporal emission profiles recorded with the PMT detection optics fixed 1 mm in front of the anode as its position relative to the capillary tip was varied. This was done by translating just the capillary, leaving the anode and the PMT detector in a fixed position. Emission from the ionization front and the residual plasma channel was more clearly resolved in this case using the 587.6 nm He $3^3\text{D}-2^3\text{P}$ transition. From a starting anode position of $z = -17$ mm, the residual channel emission was relatively unchanged while the anode was moved to about $z \sim -5$ mm. When the anode position moved closer to the capillary tip, the residual channel emission sharply increased in intensity, with a corresponding decrease in the relative intensity of the ionization front. This, at times, made it difficult to reliably discern the arrival of the ionization front near the anode when it was located close to the capillary tip (e.g. the -2 mm case in figure 3(a)). The emission in the residual channel peaked at $z \sim -2.5$ mm and disappeared with the anode located at the capillary tip, corresponding with a sharp increase in the ionization front emission intensity. This correlates with the sharp change in dynamics observed between the $z = -2$ mm and $z = 0$ mm cases in figure 3(a) and a $\sim 30\%$ increase in the average ionization front propagation speed outside the capillary with the anode at $z = 0$ mm over the speed observed with the anode at $z = -2$ mm. Thus, changes in the electrode configuration are observed to have a significant impact on the propagation dynamics of the resultant discharge, particularly with the anode located near the dielectric interface at the capillary tip. This is

visually indicated by a shift in the relative emission intensity between the ionization front and the residual plasma channel.

To further examine the effect of changing boundary conditions on discharge development, the anode was set at $z = -20$ mm and 706.5 nm emission was tracked as the ionization front passed through and out of the capillary. Selected emission profiles are shown in figure 4(a). These emission profiles correspond to the datapoints indicated by open circles in figure 3(a) at the locations indicated on the high-resolution digital photograph of the plasma jet operating at 2 kHz in figure 4(b). For most of the propagation inside the capillary, the He emission rose within ~ 15 ns and decayed usually within ~ 50 ns, indicating a rapid decrease in the rate of excitation behind the ionization front. This correlated with a relatively constant propagation speed inside the capillary. Near the anode and capillary tip, however, the decay of emission was significantly longer due to increased excitation in the residual plasma channel. At each of these locations, figure 3(a) shows locally slower discharge propagation where the residual channel emission was more pronounced, suggesting that electron energy dissipation locally increased in the residual plasma channel. This would decrease the local conductivity, resulting in a redistribution of electric potential from the ionization front into the residual channel that indirectly slows the local propagation speed of the ionization front. Near the anode, the strong intrinsic Laplacian electric field is likely supporting the enhanced energy dissipation. However, this electric field component is insignificant near the capillary tip with the anode placed at $z = -20$ mm. With similar observations to those near the anode, this suggests that a localized, *nonintrinsic* increase in electron energy dissipation in the residual plasma channel is present near the capillary tip. Figure 4(c) supports this supposition. Displayed are 706.5 nm emission profiles acquired near the anode and near the capillary tip. Emission profiles were taken from the first discharge pulse (solid line), with the oscilloscope triggered by the PMT signal, and from an averaged steady-state signal (dotted line). The residual channel emissions observed near the capillary tip in figure 4(a) was not present on the first discharge pulse, but built up with subsequent breakdowns. However, near the anode, this extended emission was observed on the first discharge pulse. This suggests that the residual channel emissions observed near the anode and near the capillary tip arise through two different mechanisms, though both act to change how the applied electric potential is distributed in the residual channel. We attribute the latter to charge accumulation on the dielectric surface between discharge pulses. This dynamic redistribution of potential in the residual streamer channel is a distinguishing property of dielectric barrier plasma jet devices that is not currently addressed in models of classical streamer formation and propagation. Figure 3(a) highlights this distinction as the streamer-like discharge assumed a more 'classical' constant propagation speed when the anode was placed at the capillary tip.

Some of the effects described in the previous figures are also manifested in the measured discharge current, shown in figure 5 with the anode positioned at $z = -20$ mm. The solid profile represents the total discharge current with the current

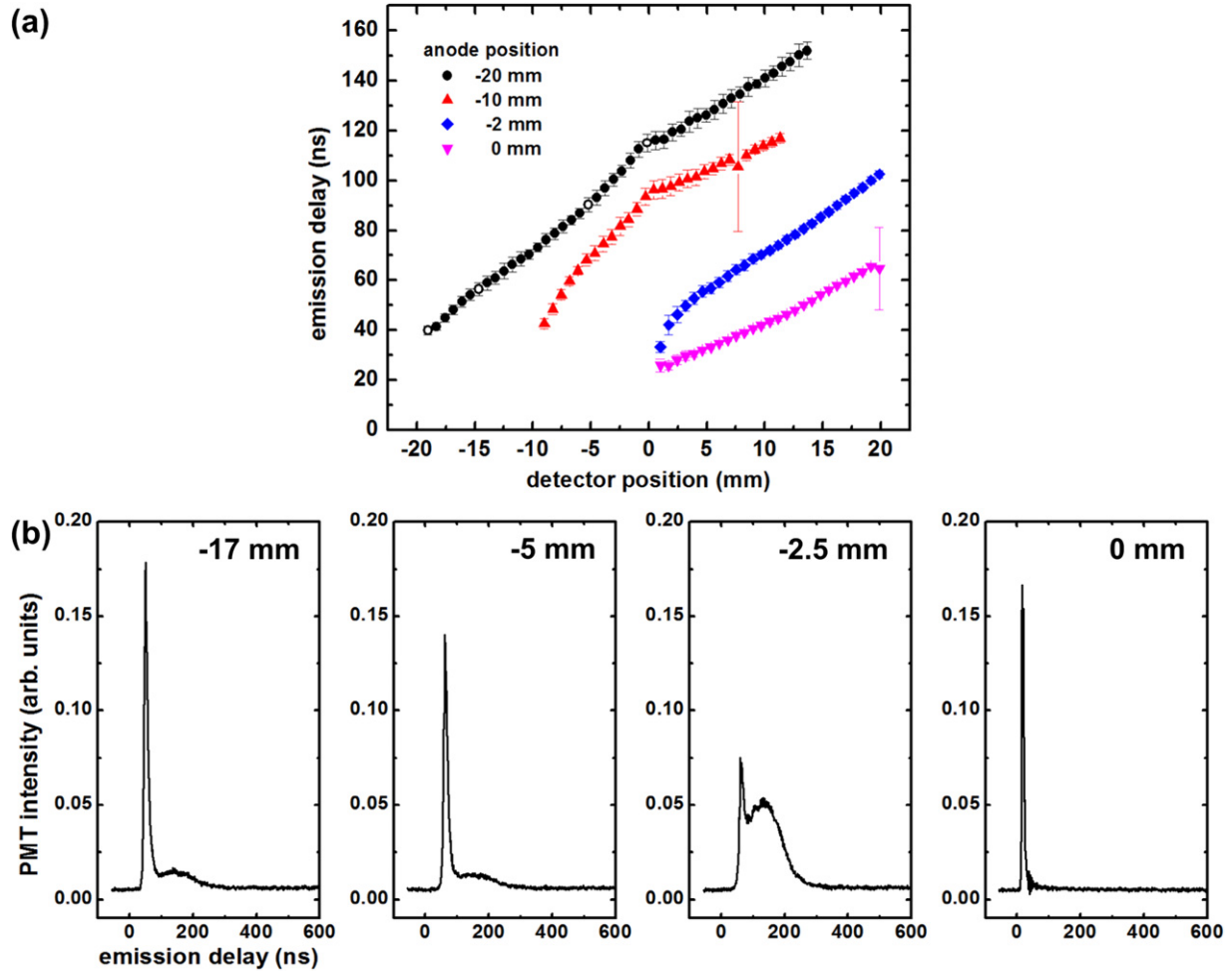


Figure 3. (a) Ionization front emission delays as a function of PMT detector position for different anode positions measured through a 10 nm bandpass filter centred at 710 nm. The capillary tip is defined at 0 mm with positive values indicating positions outside the capillary. Emission delays are referenced to the peak displacement current delay marking the rise of the applied voltage pulse. The local propagation speed is indicated by slope with steeper slopes indicating slower speeds. Error bars depict the measured temporal jitter at each point. Open circles correspond to the PMT emission profiles shown in figure 4(a). (b) Selected PMT emission profiles with the detector fixed 1 mm in front of the anode as the anode position relative to the capillary tip was varied. The data are shown from a 10 nm bandpass filter centred at 590 nm. The plasma jet was operating at 12 kV with a 2 kHz pulse repetition rate.

monitor placed at the anode (position 1 in figure 1). The dotted profile represents the current measured from the current monitor when placed just outside the capillary (position 2 in figure 1). The most notable feature in this measurement is the appearance of two distinct peaks in the total current profile. At $z = -20$ mm, these peaks were similar in amplitude. As the anode was moved closer to the capillary tip, using the same method as in figure 3(b) with the current monitor fixed at position 1 relative to the anode, figure 6(a) shows that the early peak decreased as the later peak stayed relatively constant and eventually took over when the anode was within ~ 5 mm of the capillary tip. The peak current then significantly increased when the anode was placed at the capillary tip and beyond indicating a transition away from a DBD to what was essentially a classical streamer corona discharge drawing current directly through the anode. For anode positions at $z < -20$ mm (data not shown), the current was dominated by the early peak. Figure 6(b) shows that in this region, the later peak delay increased at a roughly linear rate, much faster than for the early current peak. The later current peak

was more directly dependent on the position of the anode relative to the capillary tip. In data acquired separately from a simultaneous measurement of the relative emission intensity at the capillary tip and the total discharge current, thus avoiding the perturbative effects of the current monitor, we observed that the ionization front crossed the capillary tip around the time of the local minimum in the current shown in figure 5. Thus, the later current peak occurred as the ionization front began propagating in ambient air, slightly before the peak current was measured with the current monitor placed outside the capillary (position 2). The local increase in discharge current as the boundary conditions change outside the capillary correlates with the increase in the ionization front speed that was observed here regardless of anode position in figure 3(a) and previously by many groups.

3.3. Discharge characteristics at variable frequency

This section describes the changes that were observed in the discharge dynamics, relative emission intensity, and current

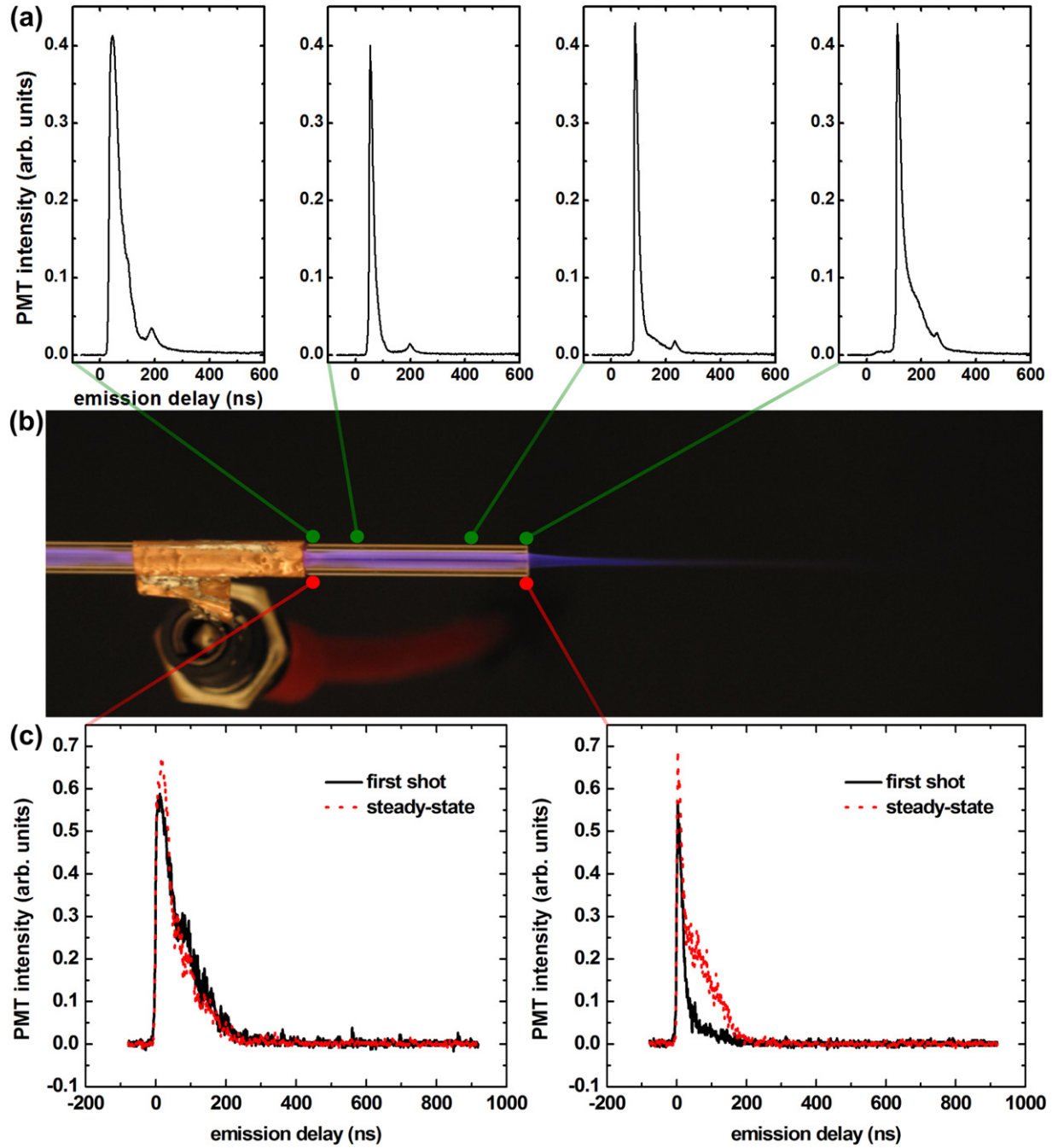


Figure 4. (a) Selected PMT emission profiles with the anode position fixed 20 mm behind the capillary tip and the position of the PMT detector variable. (b) High-resolution digital photograph of the plasma jet operating at 2 kHz. (c) PMT emission profiles from the first pulse at discharge inception (—) and the steady-state averaged emission (· · · · ·). Locations of the PMT detector in (a) and (c) are indicated in (b). The PMT data are shown from a 10 nm bandpass filter centred at 710 nm. Discharge conditions are the same as in figure 3.

as a function of pulse repetition frequency. The anode position was fixed at $z = -20$ mm. For this dataset, we could not resolve the ionization front emission from the residual channel emission close to the anode, thus the starting point was displaced a couple of millimetres from that shown in figure 3(a). Figure 7 displays the propagation dynamics at several pulse repetition frequencies measured from the 587.6 nm He $3^3\text{D}-2^3\text{P}$ transition. Open circles depict positions inside the capillary where significant emission was observed in the residual plasma channel from both 587.6

and 706.5 nm transitions. The perturbation in the ionization front propagation speed observed near the capillary tip at 2 kHz shifts back into the capillary with increasing repetition frequency. We observed this transition between 6–10 kHz, which correlates with the visually indicated transition between an annular and axial discharge morphology in figure 2. The dynamics shown at 7 and 8 kHz are representative of this transition. The perturbation can be clearly seen at $z \sim -9$ mm and -13 mm, respectively. It was characterized by a slowing of the propagation speed immediately before, followed by a quick

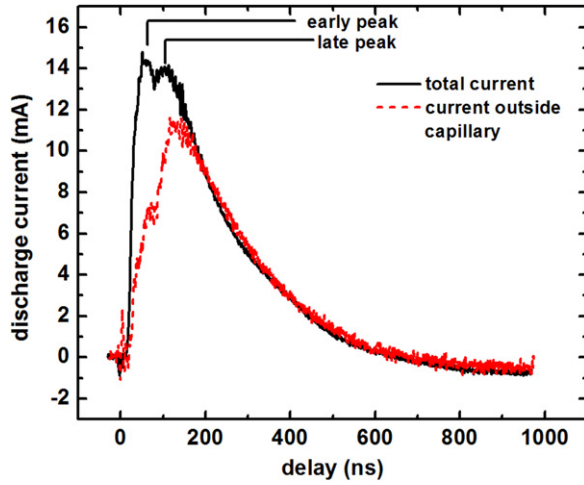


Figure 5. Measured discharge current with the current monitor located at position 1 (—) and position 2 (·····) as defined in figure 1. The anode is placed 20 mm behind the capillary tip. Discharge conditions are the same as in figure 3.

increase in the speed immediately after, very similar to what was observed at 2 kHz close to the capillary tip. The ionization front steadily decelerated following this perturbation over the rest of its propagation inside the capillary before speeding up again in ambient air at each repetition frequency. Between 6 and 10 kHz, significant residual channel emission expanded towards the anode from the capillary tip, correlating with the steadily decelerating ionization front velocity and the similar expansion of a dark wall sheath observed in figure 2. At 11 kHz, the perturbation had reached the anode and residual channel emission was observed along the entire capillary. The discharge morphology was primarily axial at this point.

The average ionization front speed in the outer jet, acquired from a linear fit to the emission delays starting at 5 mm outside the capillary, is shown in figure 8. The error bars reflect one standard deviation of the obtained linear slope. This speed sharply decreased between 2 and 6 kHz with a slower decrease up to 12 kHz. We did not acquire data for the dynamics between 2–6 kHz. Up to ~10 kHz, the opposite trend was observed for the initial propagation speed near the anode. This was evident for the cases shown in figure 7 between 2 and 7 kHz and corresponded to a sharp decrease in the discharge inception delay.

Figure 9 shows the peak 587.6 nm emission intensity from the ionization front at the repetition frequencies corresponding to the propagation dynamics shown in figure 7. Starting at 7 kHz, a localized spike in intensity can be seen shifting towards the anode as the repetition frequency was increased. The location of this intensity spike correlated with the location of the perturbation in the propagation speed. Following this intensity spike, the emission intensity steadily decreased over the remaining length of the capillary. It reached a minimum at all repetition frequencies just beyond the capillary tip before increasing again in ambient air. This increasing intensity outside the capillary is consistent with the apparent increase in conductivity noted from the measured current described in section 3.2. The emission intensity near the anode and in

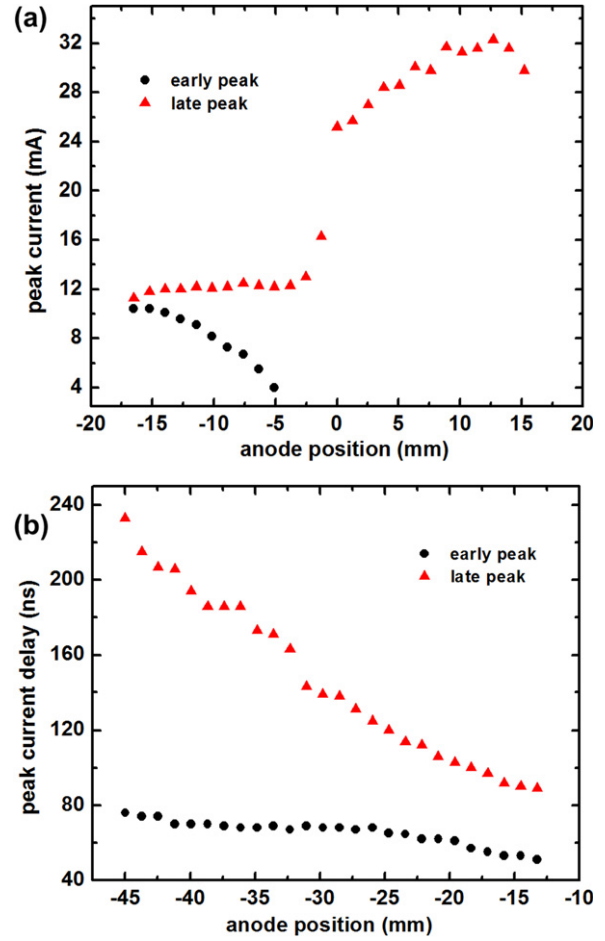


Figure 6. (a) Magnitude of the peak current for the early and late current peaks (defined in figure 5) as a function of anode position. (b) Peak current delay for the early and late current peaks as a function of anode position. Delays are referenced to the peak displacement current delay marking the rise of the applied voltage pulse. Discharge conditions are the same as in figure 3.

ambient air followed opposite trends with increasing repetition frequency, correlating with the opposing trends observed in the local propagation speeds. These trends were also reflected in the measured discharge current, for the early and late peaks, with the current monitor fixed near the anode (position 1 in figure 1) as shown in figure 10. The separate current peaks changed together up to ~6 kHz, then followed opposite trends over the transition region up to ~11 kHz before they both slowly increased at higher repetition frequencies. The total integrated charge, derived from the measured current profiles for both locations of the current monitor, steadily decreased over the measured frequency range from a peak at 2 kHz. This quantity decreased by ~10% from 2 to 15 kHz.

Figures 7–10 illustrate more clearly the effects of electric potential redistribution on the development of the plasma jet as initially described in section 3.2. When the pulse repetition frequency was increased beyond 6 kHz, the perturbation that was initially confined to the capillary tip expanded back into the capillary, corresponding to the transition in the discharge morphology that is evident in figure 2. Following this transition, the propagation dynamics and distribution of current and emission intensity were significantly altered from those

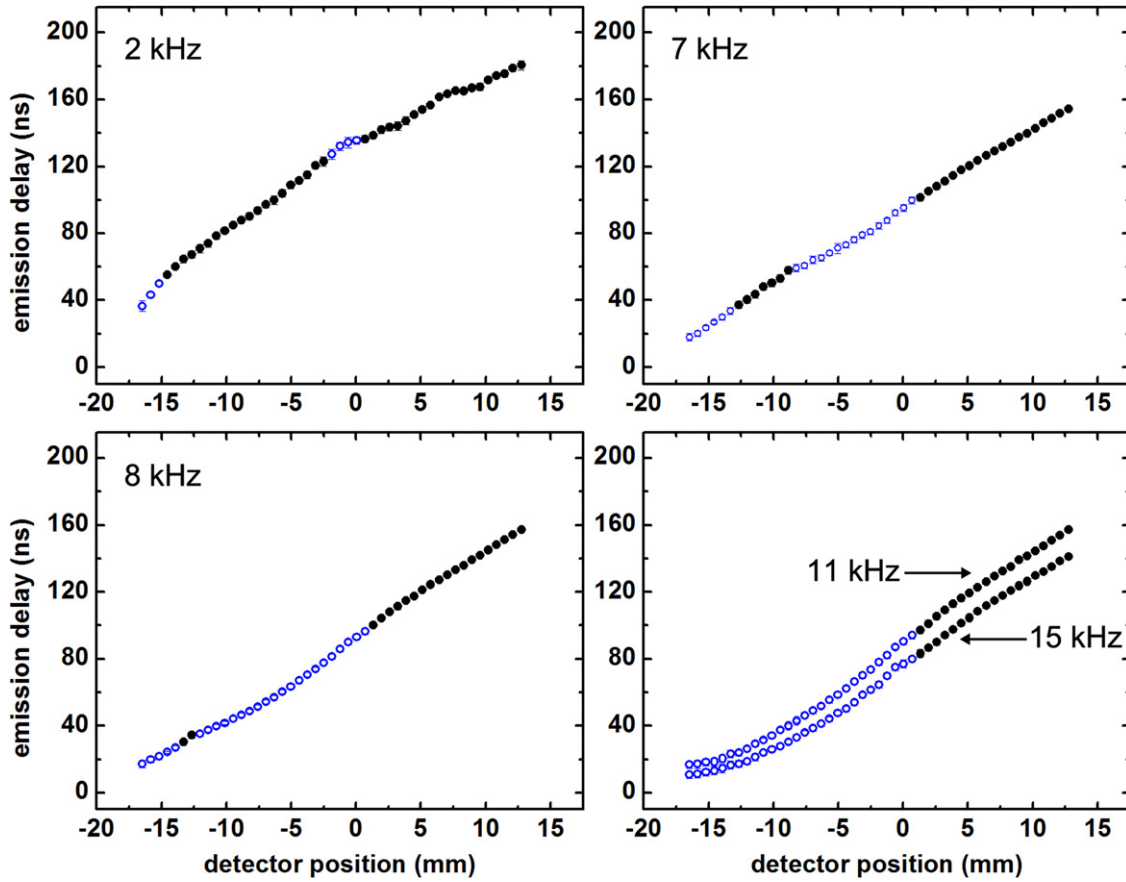


Figure 7. Ionization front emission delays as a function of PMT detector position for indicated pulse repetition frequencies at 12 kV. Definitions are the same as in figure 3. Open circles indicate positions where significant emission was observed in the residual plasma channel, otherwise, emission was observed only at the ionization front at positions indicated by closed circles. The data are shown from a 10 nm bandpass filter centred at 590 nm. The anode was placed 20 mm behind the capillary tip.

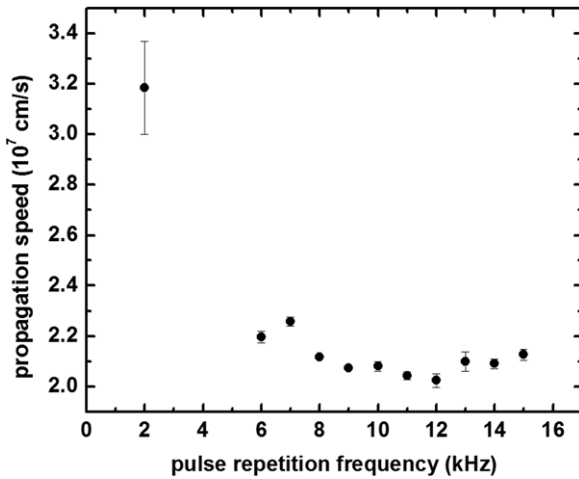


Figure 8. Ionization front propagation speed outside the capillary as a function of pulse repetition frequency. The speed was determined from a linear fit to the dataset shown in figure 7 starting at 5 mm from the capillary tip. Error bars depict one standard deviation of the linear fit.

described in section 3.2. Near the anode, the *early* peak current, ionization front emission intensity, and the local propagation speed all increased. Outside the capillary, the *late* peak current, ionization front emission intensity, and the average

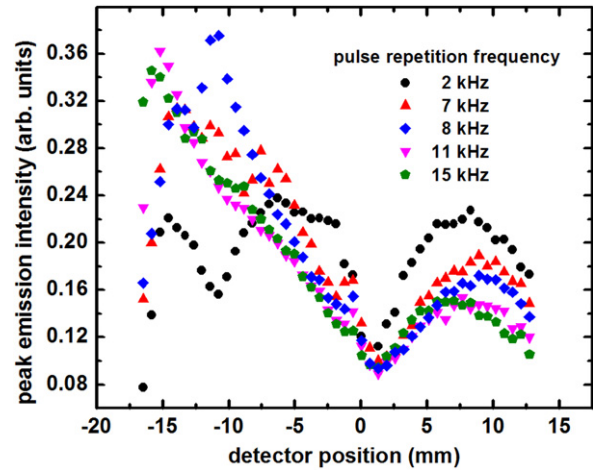


Figure 9. Ionization front peak emission intensities as a function of position. The data correspond to the dataset shown in figure 7.

propagation speed all decreased. Since the discharge seems to be initiated in an effectively higher conductivity medium at higher repetition frequencies, the potential drop between the anode region and the outer jet must be increasing to account for the observations outside the capillary. This is evident from the steady deceleration of the ionization front and decreasing

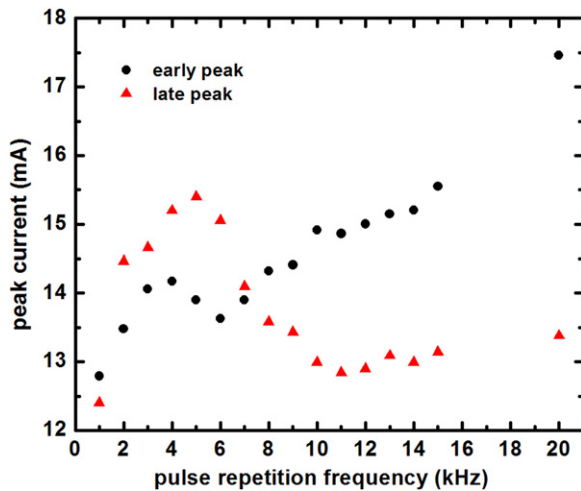


Figure 10. Peak current measured from the early and late peaks as defined in figure 5 as a function of pulse repetition frequency. The data correspond to the dataset shown in figure 7.

peak emission intensity along the capillary corresponding to the location of the axial discharge mode. This redistribution of electric potential was visually indicated by an increase in emission at 587.6 and 706.5 nm in the residual plasma channel that also correlated with the location of the axial discharge mode.

4. Discussion and conclusions

The results presented are consistent with the following phenomenological description for the development of the discharge channel in a dielectric barrier plasma jet. The developing discharge can be described by an equivalent circuit with the anode as the source of applied potential and a virtual cathode that moves with the ionization front as a source of seed electrons, through photoionization or other ionization processes. Most of the applied potential initially resides in the ionization front, but as it propagates outwards, potential is required to be distributed along the residual plasma channel due to its finite conductance. This is described by the ‘stability electric field,’ which is characteristic of the medium in which the discharge propagates. While the stability electric field has not been explicitly measured in plasma jet devices operating in He gas, a rough estimate can be gleaned from the data of Xiong *et al* (figure 3 in [26]), who found a linear relationship between plasma jet length and applied voltage when a long tube was used to exclude air from the discharge medium. The slope of the linear portion of that dataset yields an estimated electric field of $\sim 0.4 \text{ kV cm}^{-1}$. An electric field of this magnitude is consistent with the length of the backward propagating jet observed in our configuration, found to be $>20 \text{ cm}$ in length with applied voltages of 10 kV at 2 kHz. Such a low requirement for the electric field in the residual plasma channel is what enables the plasma jet to extend up to several centimetres in ambient air, as the ionization front must maintain a high potential for as long as it can before the required stability electric field in the discharge

channel eventually increases by an order of magnitude with air entrainment [3, 8].

We have shown in this paper that the distribution of electric potential along the developing discharge channel also depends significantly on the local dielectric boundary conditions. The discharge propagation dynamics were found to be a sensitive indicator of this potential distribution. With a discontinuous change in the boundary conditions at the dielectric interface, the propagation speed generally increased regardless of pulse repetition frequency or electrode configuration. This was also indicated by an increase in the local channel conductivity. Our results also show that the presence of the dielectric barrier dynamically modifies the potential distribution in the residual plasma channel. This was indicated by time-dependent changes in the discharge morphology observed with high-frame-rate imaging that correlated with a build-up of emission from the residual plasma channel following discharge inception. As the repetition frequency was increased between 6 and 10 kHz, a transition occurred whereby the balance of energy deposition shifted closer to the anode, indicating a redistribution of electric potential into the dielectric capillary. This came at the expense of the potential available to the ionization front outside the capillary resulting in a reduced propagation speed. We attribute this dynamic change in the boundary conditions to an increasing build-up of space charge on the dielectric surface that does not fully recombine before the next discharge pulse. This excess space charge appears to be concentrated near the capillary tip and distributed along the inner wall of the capillary. As the repetition frequency is increased, the threshold density of surface charge sufficient to impact the development of the discharge is surpassed further inside the capillary, resulting in the observed transition in discharge behaviour. The energy lost per pulse due to charging of the dielectric surface is perhaps evident in the $\sim 10\%$ decrease in integrated charge measured from the current between 2 and 15 kHz. The effects described in this paper were observed to be significantly dependent on the external circuit configuration. When we reduced the applied voltage to 6 kV, closer to the breakdown threshold, the potential redistribution effect was much more significant and was additionally marked by a decreasing jet length with increasing repetition frequency. We also observed that the range of repetition frequencies where the discharge morphology and dynamics transitioned depended on the applied voltage pulse shape.

This experiment underscores the need to account for effects arising from the interaction of the dielectric barrier with the plasma channel when modelling discharge development in the dielectric barrier plasma jet, particularly at high-repetition rates. Recent modelling results appear to describe the morphology of the discharge inside the capillary at least for the initial breakdown pulse under our conditions. However, our results show that the dielectric boundary conditions can be very quickly altered inside the capillary with increasing repetition frequency. To understand how dielectric barrier plasma jets can be optimized for applications in a particular configuration, the entire circuit formed by the developing discharge needs to be considered.

Acknowledgments

This material is based upon work supported by the Air Force Office of Scientific Research under Contract Award No FA8650-04-D-2404, in cooperation with the Wright State University Center for Advanced Power and Energy Conversion.

References

- [1] Teschke M, Kedzierski J, Finantu-Dinu E G, Korzec D and Engemann J 2005 *IEEE Trans. Plasma Sci.* **33** 310–11
- [2] Morrow R and Lowke J J 1997 *J. Phys. D: Appl. Phys.* **30** 614–27
- [3] van Veldhuizen E M and Rutgers W R 2002 *J. Phys. D: Appl. Phys.* **35** 2169–79
- [4] Lu X and Laroussi M 2006 *J. Appl. Phys.* **100** 063302
- [5] Sands B L, Ganguly B N and Tachibana K 2008 *Appl. Phys. Lett.* **92** 151503
- [6] Ye R and Zheng W 2008 *Appl. Phys. Lett.* **93** 071502
- [7] Shi J, Zhong F, Zhang J, Liu D W and Kong M G 2008 *Phys. Plasmas.* **15** 013504
- [8] Raizer Y 1991 *Gas Discharge Physics* (Berlin: Springer)
- [9] Mericam-Bourdet N, Laroussi M, Begum A and Karakas E 2009 *J. Phys. D: Appl. Phys.* **42** 055207
- [10] Li Q, Li J T, Zhu W C, Zhu X M and Pu Y K 2009 *Appl. Phys. Lett.* **95** 141502
- [11] Urabe K, Ito Y, Sakai O and Tachibana K 2010 *Japan. J. Appl. Phys.* **49** 106001
- [12] Xiong Q, Lu X, Xian Y, Jiang Z and Pan Y 2010 *J. Appl. Phys.* **108** 103303
- [13] Algwari Q Th and O'Connell D 2011 *Appl. Phys. Lett.* **99** 121501
- [14] Xiong Q, Lu X, Liu J, Xian Y, Xiong Z, Zou F, Zou W, Gong C, Hu J and Chen K 2009 *J. Appl. Phys.* **106** 083302
- [15] Jiang C, Chen M T and Gundersen M A 2009 *J. Phys. D: Appl. Phys.* **42** 232002
- [16] Jarrige J, Laroussi M and Karakas E 2010 *Plasma Sources Sci. Technol.* **19** 065005
- [17] Karakas E and Laroussi M 2010 *J. Appl. Phys.* **108** 063305
- [18] Breden D, Miki K and Raja L L 2011 *Appl. Phys. Lett.* **99** 111501
- [19] Jánský J and Bourdon A 2011 *Appl. Phys. Lett.* **99** 161504
- [20] Jánský J, Le Delliou P, Tholin F, Tardiveau P, Bourdon A, and Pasquiers S 2011 *J. Phys. D: Appl. Phys.* **44** 335201
- [21] Sakiyama Y, Graves D B, Jarrige J and Laroussi M 2010 *Appl. Phys. Lett.* **96** 041501
- [22] Naidis G V 2011 *Appl. Phys. Lett.* **98** 141501
- [23] Naidis G V 2010 *J. Phys. D: Appl. Phys.* **43** 402001
- [24] Vision Research Inc., www.visionresearch.com
- [25] Frost M J, Himmelmann S and Palmer D D 2001 *J. Phys. B: At. Mol. Opt. Phys.* **34** 1569–87
- [26] Xiong Q, Lu X, Ostrikov K, Xiong Z, Xian Y, Zhou F, Zou C, Hu J, Gong W and Jiang Z 2009 *Phys. Plasmas.* **16** 043505